RSC Advances

PAPER

View Article Online
View Journal | View Issue

Cite this: *RSC Adv.*, 2019, **9**, 11737

Development of moisture-proof polydimethylsiloxane/aluminum oxide film and stability improvement of perovskite solar cells using the film†

Eun Young Choi,[a] Ju-Hee Kim,[a] Bu-Jong Kim,[a] Ji Hun Jang,[a] Jincheol Kim*[ab] and Nochang Park*[a]

Received 12th February 2019
Accepted 8th April 2019

DOI: 10.1039/c9ra01107b

rsc.li/rsc-advances

A method for enhancing the moisture barrier property of polydimethylsiloxane (PDMS) polymer films is proposed. This is achieved by filling the PDMS free volume with aluminum oxide (AlO_x). To deposit AlO_x inside PDMS, thermal atomic layer deposition (ALD) is employed. The PDMS/AlO_x film thus produced has a 30 nm AlO_x layer on the surface. Its water vapor transmission rate (WVTR) is 5.1×10^{-3} g m^{-2} d^{-1} at 45 °C and 65% relative humidity (RH). The activation energy of permeability with the PDMS/AlO_x film for moisture permeation is determined to be 35.5 kJ mol^{-1}. To investigate the moisture barrier capability of the PDMS/AlO_x layer, $(FAPbI_3)_{0.85}(MAPbBr_3)_{0.15}$/spiro-OMeTAD/Au perovskite solar cells are fabricated, and encapsulated by the PDMS/AlO_x film. To minimize the thermal damage to solar cells during ALD, AlO_x deposition is performed at 95 °C. The solar cells exposed to 45 °C-65% RH for 300 h demonstrate less than a 5% drop in the power-conversion efficiency.

Introduction

Recently, solar cell encapsulation employing organic–inorganic halide perovskite solar cells (PSCs) to overcome instability in the presence of moisture has gained considerable attention.[1–4] Recently, various methods, such as using UV curable epoxy[5] and moisture barrier film[3,6] to protect the PSCs from moisture have been proposed, which show encouraging results under high humidity.[7–11] The previous studies reported that encapsulated PSCs using an organic layer start degrading from perovskite decomposition when moisture penetrates the organic layer.[5,12–14] To overcome this, atomic layer deposition (ALD) is used as one of the effective techniques to fabricate oxide thin films on the device. Furthermore, researchers reported the results of the water vapor transmission rate (WVTR) of oxide films fabricated by ALD. Wang *et al.* reported the use of ALD to fabricate Al_2O_3/MgO, which when coupled with solution-processed polymer, achieved a high moisture barrier and has a superior WVTR of 1.05×10^{-6} g m^{-2} d^{-1} at 60 °C-100% RH.[15] Nam *et al.* obtained a WVTR of 2×10^{-3} g m^{-2} d^{-1} at 85 °C-85% RH using a composite layer of ALD Al_2O_3 and chemical-vapor-deposited graphene.[16] We achieved a WVTR of 1.84×10^{-2} g m^{-2} d^{-1} at 45 °C-100% RH when thermal ALD is used.[17] Based on our previous research,[17] a low process temperature of ALD and a method to enhance the WVTR are required to be used in PSCs. For low damage of PSCs during ALD, we performed ALD at a temperature as low as 95 °C. However, we observed that it is difficult to achieve the high moisture barrier property with a single Al_2O_3 film. Therefore, previous researchers employed organic materials to enhance the moisture barrier property. Park *et al.* introduced the thin film encapsulation method for OLED devices by coating polydimethylsiloxane (PDMS) on metal foil. They reported a WVTR of 4.4×10^{-4} g m^{-2} d^{-1} at 45 °C-40% RH.[18] Similarly, Hong *et al.* introduced flexible lamination encapsulation using graphene films with PDMS on polyethylene terephthalate (PET).[19] Liu *et al.* developed a hole transport material (HTM)-free PSC by using a carbon electrode and performing PDMS encapsulation. They reported long-term stability of PSCs in low-humidity conditions at room temperature for 3000 h.[20] We summarized the related works in Table S1.† However, those results lacked the investigation of how the WVTR was increased using an organic layer. Therefore, first, we focused on a method to improve the moisture barrier property by combining PDMS and AlO_x. Second, we investigated why the WVTR is enhanced when the PDMS/AlO_x double layer is used. PDMS is employed because of its low cost,[21] chemical stability,[22] easy process to fabricate film or mold,[23] high transparency,[24] and common usage in the microfluidic cell[25–27] and other devices.[28,29] In addition, it exhibits the hydrophobic property.[30]

[a]*Electronic Convergence Material & Device Research Center, Korea Electronics Technology Institute, Seong-Nam, Republic of Korea. E-mail: ncpark@keti.re.kr; jckim@keti.re.kr; Tel: +82-31-789-7057*

[b]*Australian Centre for Advanced Photovoltaics (ACAP), School of Photovoltaic and Renewable Energy Engineering, University of New South Wales, Sydney 2052, Australia*

† Electronic supplementary information (ESI) available. See DOI: 10.1039/c9ra01107b

However, these results lack the investigation of how the WVTR was increased using an organic layer.

The objectives of the research reported in this study are: (1) to develop a method of enhancing the moisture barrier property of the PDMS by employing AlO_x thin film; (2) to determine the WVTR of the PDMS/AlO_x film by the Ca corrosion test, and to investigate the mechanism that improves the WVTR; (3) and to investigate the stability of PSCs encapsulated by the PDMS/AlO_x moisture barrier film. Accordingly, we fabricated three types of films: (a) AlO_x, (b) AlO_x/PDMS, and PDMS/AlO_x (Fig. S1†). To examine the effectiveness of the moisture barrier film, we encapsulated the perovskite solar cell, $(FAPbI_3)_{0.85}(MAPbBr_3)_{0.15}$/spiro-OMeTAD/Au, by these films.

Results and discussion

Effect of TMA and water pulse time on the deposition rate of AlO_x thin film

We investigated if TMA and water pulse times affect the growth rate of the AlO_x film. Fig. 1a shows that the growth rate per cycle (GPC) of the AlO_x film is in the 1.20–1.38 Å range with the change in TMA pulse time from 0.5 s to 3.0 s. Further, we examined the effect of water pulse time on the GPC of the AlO_x film.

Fig. 2b shows that the GPC of the AlO_x film doubled in 3 s water pulse time as compared to that obtained with 0.5 s water pulse time. This is attributed to precursor decomposition.[31] Based on these results, we determined the GPC in accordance with the number of ALD cycles. Fig. 2a illustrates that the slope is 1.09 Å per cycle, which means the AlO_x film grows linearly in a positive relationship with the ALD cycles. To examine the thickness, we employed transmission electron microscopy (TEM) and energy dispersive spectroscopy (EDS) analysis after 200 cycles (Fig. 2b and c). These figures indicate that the AlO_x films formed uniformly on the substrate and consisted of Al and O. The presence of oxygen in the substrate is attributed to oxidation.[32] Therefore, we observed that the thickness of AlO_x films could be determined by changing the ALD cycles at fixed TMA and water pulse times.

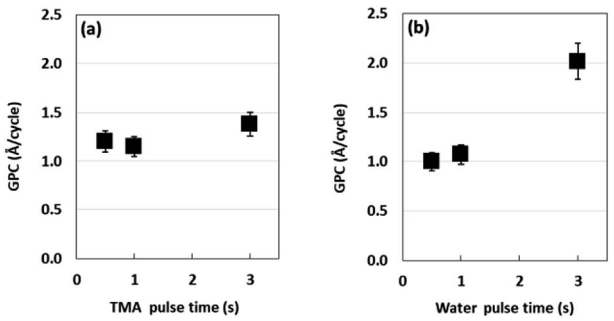

Fig. 1 Effect of (a) TMA pulse time and (b) water pulse time on the growth rate of AlO_x thin films. Si wafer substrates were used to form the AlO_x thin film. The ALD process was performed at 95 °C for 100 cycles.

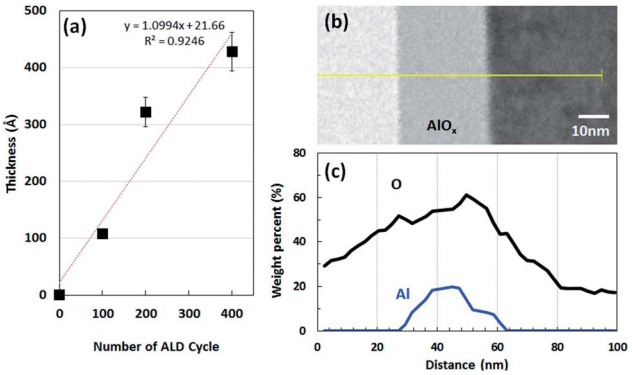

Fig. 2 (a) Thickness of AlO_x thin films as a function of number of ALD cycles. (b) TEM image of 30 nm AlO_x layer that is formed by using condition C in Table 1. (c) EDS element line scan results of the yellow line in (b).

Once the AlO_x thin films were formed by ALD process, we used an X-ray photoelectron spectra (XPS) to ensure the stoichiometric ratio of Al and O. Correlation factors (R^2) of devolution fitting in Fig. 3(a) and (b) were 0.995, 0.999, respectively. Fig. 3a shows the Al 2p spectra of AlO_x with Gaussian fitting. It is distributed by one component at the 74.45 eV, which corresponds to Al–O.[32] Fig. 3b shows that the O 1s spectra of AlO_x consist of two peaks, which correspond to Al–O and Al–OH bonds at 531.29 eV and 532.60 eV, respectively.[33] On the base of peak devolution of each element, we determined the stoichiometric ratio of the fabricated film by ALD. We chose the peak area of Al–O bonding from the devolved Al 2p and O 1s spectra, and used the element-specific cross sections of Al 2p and O 1s.[33,34] The results demonstrated that the stoichiometric ratio of [O/Al] was 1.38 (Table S3†)

PDMS film filled with AlO_x and its WVTR

Based on our previous study and other research findings,[35–38] the AlO_x thin film requires other layers for enhancing the moisture barrier property. For this experiment, we used PDMS as the organic layer. To cure a PDMS layer, it was heated at 95 °C for 1 h after spinning coating. This temperature corresponds to the temperature of ALD process. This allowed the PDMS to be cured further in the ALD chamber. The subsequent step was to deposit AlO_x. After the formation of each layer, we examined the quality of the layer, especially the WVTR and contact angle.

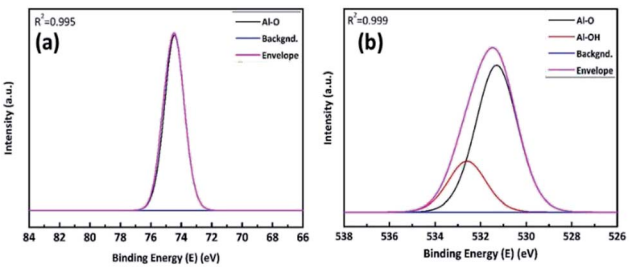

Fig. 3 XPS spectra of AlO_x thin films on Si wafer. (a) Al 2p and (b) O 1s.

First, we investigated the effect of filling AlO_x with free volume in PDMS on the WVTR. Fig. 4 show that the lag time of the Ca/PDMS/AlO_x film was approximately twice as that of Ca/AlO_x/PDMS, which are measured to be 19.71 h and 8.01 h, respectively. The WVTR values of the PDMS/AlO_x and AlO_x/PDMS film are determined to be 5.10×10^{-3} g m^{-2} d^{-1} and 1.46×10^{-2} g m^{-2} d^{-1}, respectively (refer Table 1). The WVTR value of a 30 nm AlO_x film was determined to be 2.89×10^{-2} g m^{-2} d^{-1}, which is in good agreement with 1.84×10^{-2} g m^{-2} d^{-1} (what we had done with AQUATRON model 2 (Mocon) before).[17] Interestingly, the WVTR value was decreased by orders of 10^{-1} when we performed AlO_x deposition on the PDMS layer. To examine the reason of enhancing the moisture barrier property, we employed TEM/EDS, ToF-SIMS, and XPS. First, we will explain the TEM results and then discuss the ToF-SIMS and XPS results.

For the Si/AlO_x/PDMS sample (Fig. 5a), EDS mapping results showed clear distinctions in the AlO_x and the PDMS layers. Moreover, for the Si/PDMS/AlO_x sample (Fig. 5b), Al was detected in the PDMS layer. We employed TOF-SIMS to analyze the elements inside the PDMS layer more precisely. Fig. 6 shows that Al exists from the surface to several hundred nanometers. To make sure that Al exists in the PDMS layer, we performed XPS analysis. Fig. 7a and b can be devaluated with Gaussian fitting whose correlation factors were 0.999 and 0.996 each. Fig. 7a illustrates the binding energy of Al 2p of the PDMS/AlO_x film. The spectra was obtained at 74.45 eV and 75.2 eV, which represents Al–O and Al–OH bonds, respectively.[32] Interestingly, unlike the Al 2p peak of AlO_x reference, the peak area of the Al–OH bond for PDMS/AlO_x occupies in the total 2p peak. The diffusivity and miscibility of the ALD precursor is related to the free volume of polymer,[39] reactive site of polymer,[40] and polymer porosity and crystallinity.[41,42] These results are affected by the intrinsic property of the PDMS such as its crystallinity and reactivity[43] and are similar to those of polyethylene ethoxylate (PEIE), whose semi-crystalline nature affects the retarded nucleation of the ALD layer.[44] Fig. 7b shows the O 1s spectra of the PDMS/AlO_x film. The Al–O spectra and Al–OH were detected at 531.29 eV and 532.60 eV, which are from the AlO_x layer. As shown in Fig. S4,† the peak related to AlO_x layer, where the peak between 3400 cm^{-1} and 3000 cm^{-1} were attributed to stretching vibrations of Al–OH[45] and the peak of 1000 cm^{-1} was corresponded to Al–O stretching vibrations.[46] The other spectra peak of 533.0 eV represent the binding energies of O–Si–O.[47] These spectra peaks is from the PDMS layer supported by results from FTIR (Fig. S4†), which shows the peak at 1090 cm^{-1} were attributed to Si–O–Si stretching vibration in PDMS bone structure.[48] An AlO_x cluster forms in the void inside the PDMS layer during ALD process.[39,44,49,50] Therefore, our results demonstrated that the moisture barrier property of the PDMS/AlO_x film was improved by filling the free volume in PDMS layer with AlO_x.

Table 1 Calculated WVTR and lag time of AlO_x, AlO_x/PDMS, and PDMS/AlO_x at 45 °C and 65% RH

Sample	WVTR (g m^{-2} d^{-1})	Lag time (h)
AlO_x	2.89×10^{-2}	0.86
AlO_x/PDMS	1.46×10^{-2}	8.01
PDMS/AlO_x	5.10×10^{-3}	19.71

Second, we investigated the effect of AlO_x and PDMS on surface properties, such as contact angle and surface tension.[51] The permeation of water molecules is related to the wettability of the barrier thin film. Fig. 8 shows that the hydrophobicity was improved by forming the PDMS layer on the AlO_x thin film. The contact angle and surface tension of the AlO_x/PDMS sample was determined to be 86.8° and 30.0 mN m^{-1}, respectively (refer Table 2). These results are attributed to the chemical structure of PDMS, which have the methyl functional group.[52] Interestingly, the contact angle of AlO_x increased from 60.8 to 74.1 when PDMS was used in the lower layer of the AlO_x thin film. In general, the surface energy is concerned with the atom arrangement of surface and inside, which means that the measured contact angle

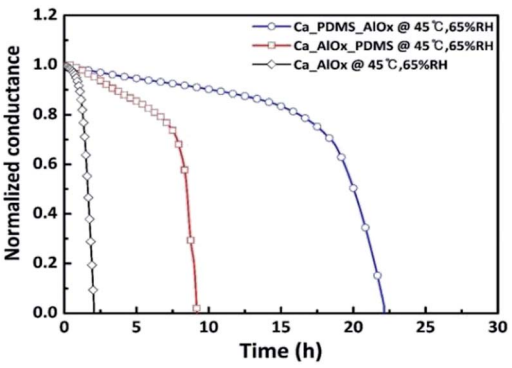

Fig. 4 Ca conductance test encapsulated by three types of materials: AlO_x, PDMS/AlO_x, and AlO_x/PDMS. This test was conducted at 45 °C and 65% RH.

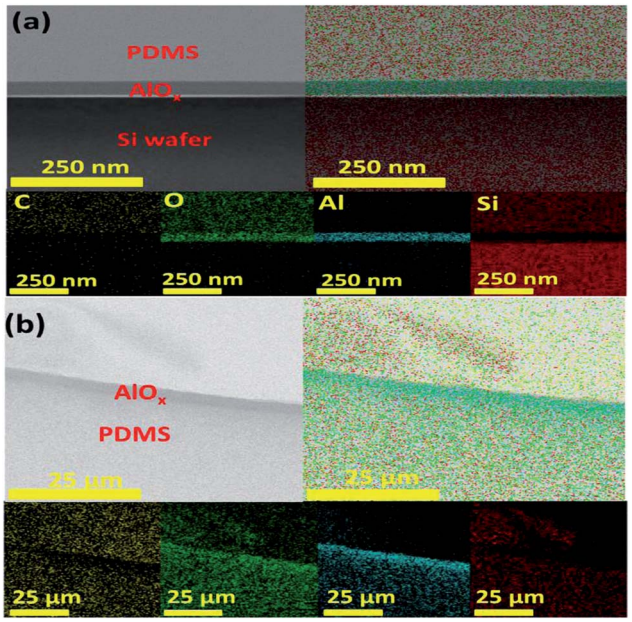

Fig. 5 TEM images and EDS elemental mapping (C, O, and Al, Si) of (a) AlO_x/PDMS and (b) PDMS/AlO_x.

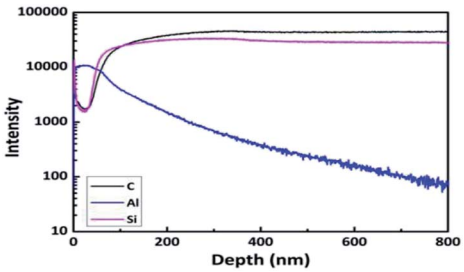

Fig. 6 ToF-SIMS depth profile of Si/PDMS/AlO$_x$.

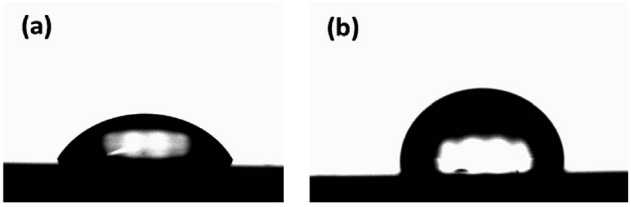

Fig. 7 Si/PDMS/AlO$_x$ XPS spectra of (a) Al 2p and (b) O 1s.

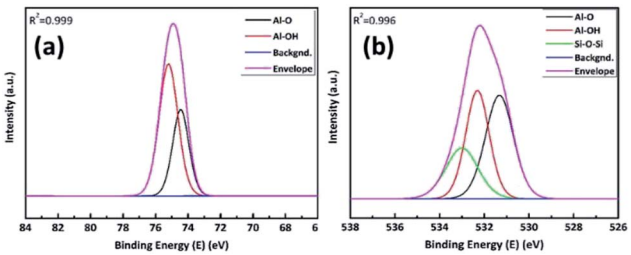

Fig. 8 Contact angles of (a) Si/AlO$_x$ and (b) Si/AlO$_x$/PDMS using water.

indicates the growth formation of films according to the deposition condition.[53] Therefore, the difference of surface energy with PDMS/AlO$_x$ indicated that the surface and internal arrangements of AlO$_x$ changed *via* deposition on PDMS, which corresponded with TEM-EDS and SIMS results.

Effect of temperature on the WVTR of PDMS/AlO$_x$ thin film

The WVTR value is dependent on the temperature and relative humidity.[54,55] To examine the relationship between temperature and WVTR values, the Ca/AlO$_x$ and Ca/PDMS/AlO$_x$ samples were stored at three different temperatures: 25 °C, 45 °C, and 65 °C. The RH was maintained at 65%. The change in conductance was also monitored. Fig. 9 shows that the lag time increases as the temperature decreases to 25 °C. The result demonstrated that the moisture passage through the film was slow at low temperature. To quantify the moisture barrier property, the WVTR values were determined under each condition (see Table 3). In addition, we determined the activation energy of permeability of the Ca/AlO$_x$ and Ca/PDMS/AlO$_x$ films for permeation as using the following equation.[55,56]

$$\mathrm{WVTR} = \mathrm{WVTR_o} \times \exp(-E_a/RT), \quad (1)$$

where WVTR$_o$ is a constant dependent on the system, E_a is the activation energy for permeation, and R is the gas constant (8.314 J K^{-1} mol^{-1}). The activation energy was determined using the linear slope from the graph of ln WVTR *versus* $1/RT$. The activation energies of permeability and correlation factors (R^2) of AlO$_x$ and PDMS/AlO$_x$ were determined to be 30.0 kJ mol^{-1} (R^2 = 0.98) and 35.5 (R^2 = 0.91) kJ mol^{-1}, respectively, as shown in Fig. 10. The activation energy of the PDMS/AlO$_x$ film is greater than that of AlO$_x$ film, which indicates it takes longer time for moisture permeation through the PDMS/AlO$_x$ film than AlO$_x$ film.[57–60]

PDMS/AlO$_x$ encapsulation for PSCs

Finally, we fabricated the $(FAPbI_3)_{0.85}(MAPbBr_3)_{0.15}$/spiro-OMeTAD/Au solar cells, which are encapsulated by two kinds of films: (a) AlO$_x$ and (b) PDMS/AlO$_x$. The solar cells were subjected to environmental test to examine their stabilities in terms of changes in power conversion efficiency (PCE). Although AlO$_x$- and encapsulated solar cells suffered over 15% drop in PCE (see Fig. S2† for the degradation), but there were only below 5% PCE drop for the PDMS/AlO$_x$-encapsulated devices at 45 °C in 65% RH for 300 h as shown in Fig. 11. This result shows better long-term stabilities compared to our previous report.[61]

To investigate the main cause of the degradation in our devices, we conducted further experiment at room temperature

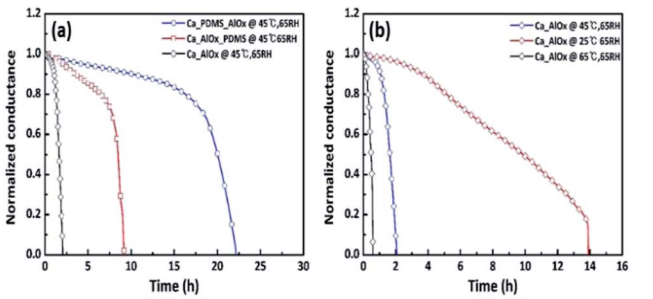

Fig. 9 Ca electrical test results of (a) PDMS/AlO$_x$ and (b) AlO$_x$ at 65% RH in accordance with the temperature.

Table 2 Contact angle and surface tension of Si/AlO$_x$, Si/AlO$_x$/PDMS and Si/PDMS/AlO$_x$

Sample	DI [°]	CH_2I_2 [°]	Polar [mN m^{-1}]	Disp. [mN m^{-1}]	Surface tension [mN m^{-1}]
AlO$_x$	60.8	47.8	17.1	27.0	44.1
AlO$_x$/PDMS	86.8	58.8	3.9	26.1	30.0
PDMS/AlO$_x$	74.1	58.4	10.8	23.5	34.2

Table 3 Contact angle and surface tension of Si/AlO_x, Si/AlO_x/PDMS and Si/PDMS/AlO_x

Sample	WVTR (g m^{-2} d^{-1})	Lag time (h)	Measurement condition
PDMS/AlO_x	3.11×10^{-3}	32.29	25 °C and 65% RH
PDMS/AlO_x	5.10×10^{-3}	19.71	45 °C and 65% RH
PDMS/AlO_x	2.18×10^{-2}	9.16	65 °C and 65% RH
AlO_x	1.35×10^{-2}	6.01	25 °C and 65% RH
AlO_x	2.89×10^{-2}	0.86	45 °C and 65% RH
AlO_x	6.10×10^{-2}	0.26	65 °C and 65% RH

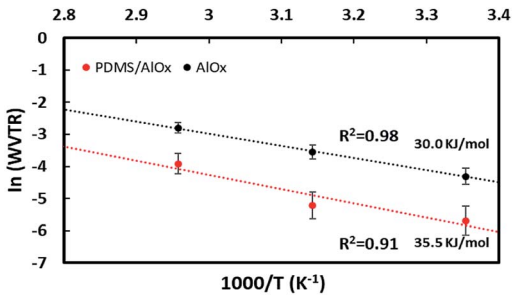

Fig. 10 Plots of the ln(WVTR) *versus* temperatures for AlO_x and PDMS/AlO_x.

in 65% RH condition with our PDMS/AlO_x-encapsulated devices. As shown in Fig. S5,† the PDMS/AlOx encapsulated PSCs were rarely degraded even though these perovskite cells were exposed in high humidity at room temperature. It should be noted that the perovskite cells with PDMS/AlOx encapsulation layer showed PCE drop about 5% at 45 °C in 65% RH. Therefore, the main degradation mechanism on our devices is likely thermal degradation at spiro-OMeTAD layer as also reported in other literature.[61] In other words, These results indicate that the PDMS/AlO_x layer is effective in preventing moisture, but there are still rooms to investigate in the future for finding a good hole transport layer candidate to ensure long-term stability of perovskite solar cells.

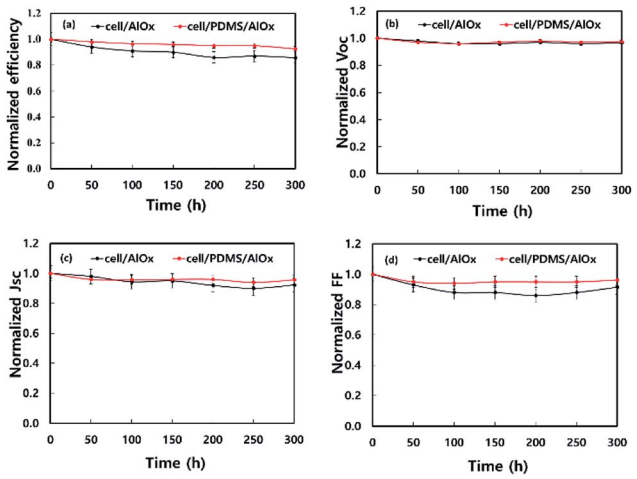

Fig. 11 Evolution of (a) PCE, (b) V_{oc}, (c) J_{sc} and (d) fill factor of perovskite photovoltaic cells with AlO_x or PDMS/AlO_x at 45 °C and 65% RH condition. Error bar is standard deviation.

Conclusions

This study focused on a method to enhance the moisture barrier property and WVTR of the AlO_x thin film using PDMS. In addition, this study demonstrated the use of PDMS/ALD 30 nm AlO_x layer on top of PSCs as an encapsulant to improve the stability by preventing moisture ingress. We observed that AlO_x filled the vacancy in the PDMS layer when the AlO_x thin films formed on the PDMS layer *via* ALD. That makes it difficult for moisture to permeate the film, which results in the enhancement of moisture barrier property. We deposited three types of thin films on the Ca film to examine the moisture barrier property. These include (a) AlO_x, (b) AlO_x/PDMS, and (c) PDMS/AlO_x. The WVTR values of PDMS/30 nm AlO_x layers by optimized thermal ALD process at a temperature as low as 95 °C was measured to be 5.1×10^{-3} g m^{-2} d^{-1} at 45 °C-65% RH. The activation energies for moisture permeation of the AlO_x and PDMS/AlO_x films were determined to be 30.0 kJ m^{-1} and 35.5 kJ mol^{-1}, respectively. We observed that the PDMS/AlO_x film was more hydrophobic than the AlO_x film. This is attributed to the low surface tension of PDMS film. Finally, we fabricated the $(FAPbI_3)_{0.85}(MAPbBr_3)_{0.15}$/spiro-OMeTAD/Au perovskite solar cells and encapsulated it by two types of thin films. These include AlO_x and PDMS/AlO_x. The PDMS/AlO_x-encapsulated solar cells experienced less than 8% drop in PCE after 300 h of 45 °C-65% RH. In contrast, the AlO_x-encapsulated devices showed over 15% drop of PCE at 45 °C-65% RH. This is mainly attributed to thermal degradation of spiro-OMeTAD. With further development in the moisture barrier property of the AlO_x film by employing the PDMS layer, we propose that the ALD process is an excellent approach to encapsulate perovskite solar cells.

Experimental section

Experimental apparatus

In this experiment, we designed an ALD system that is connected to a glove box. A thermal evaporator was installed inside the glove box, which can handle calcium (Ca) in a nitrogen condition. We formed the Ca layer on a glass using thermal evaporator, and then coated the PDMS on the Ca layer using a spin coater (Ca/PDMS). After curing the PDMS, the samples were placed in the ALD chamber to deposit AlO_x. The whole process was performed in nitrogen environment. Each condition of this experiment is explained in detail in the next section.

Ca cell fabrication and characterization

Ca cell fabrication. The 300 nm Ca film was formed on a glass substrate (2.5 cm × 2.5 cm) using thermal evaporator. After Ca deposition, the 200 nm Al electrode was deposited onto the glass *via* evaporator (Fig. 1a). The next step is to encapsulate the Ca samples. For this, the Ca samples were divided into three groups, as shown in Fig. 1. These include (a) AlO_x deposition

(Ca/AlO_x), (b) AlO_x deposition and then PDMS coating (Ca/AlO_x/PDMS), and (c) PDMS coating and then AlO_x deposition (Ca/PDMS/AlO_x). PDMS (Sylgard 184, Sigma Aldrich) was used in this study. The silicone elastomer was mixed with a curing agent in a 10 : 1 ratio by weight. The PDMS was coated at 1000 rpm for 30 s. Further, it was annealed at 95 °C for 1 h. The thickness of PDMS was measured to be about 55 μm(see Fig. S3†).

ALD deposition condition. We employed a thermal ALD process (model: IH-10, ITECHU, South Korea) in this study. The ALD procedure consists of four steps: (1) the TMA precursor was pulsed into reaction chamber, (2) Ar gas was purged to clean the reaction chamber, (3) H_2O reactant was pulsed into reaction, and (4) excess reactant was removed from reaction chamber by Ar purging. To make sure of deposition thickness of AlO_x, we investigated the effect of two factors on the deposition rate: (1) TMA pulse time and (2) water pulse time. The test conditions are summarized in Table S2.† Further, we examined the relationship between ALD cycles and AlO_x thickness.

Characterization of Ca cell. The Ca cells were placed in three different temperature–humidity conditions: (a) 25 °C-65% RH, (b) 45 °C-65% RH, and (c) 65 °C-65% RH. The change in conductance (G) was measured in each condition (Keithley 2400 multimeter). Using the change in G, we determined the WVTR values using the equation stated in ref. 62.

$$\mathrm{WVTR} = -2\left(\frac{M_{\mathrm{H_2O}}}{M_{\mathrm{Ca}}}\right)\rho_{\mathrm{Ca}}\sigma\left(\frac{\mathrm{d}(G)}{\mathrm{d}(t)}\right)\left(\frac{A_{\mathrm{Ca}}}{A}\right), \quad (2)$$

where 2 is the molar equivalent of Ca corrosion reaction, M_{H_2O} (18 g mol^{-1}) and M_{Ca} (40.1 g mol^{-1}) are the molecular weights of water and Ca, respectively, ρ_{Ca} (1.55 g cm^{-3}) is the density of Ca, σ (3.4×10^{-8} Ω m) is the resistivity of Ca, $\frac{d(G)}{\mathrm{d}(t)}$ is the rate of conductance (G) change, A_{Ca} is the area of deposited Ca, and A is the barrier film area on Ca.

Perovskite solar cell fabrication and characterization

Materials

(1) Synthesis of perovskite absorption materials. (a) To synthesize $HC(NH_2)_2I$, 15 g formamidine acetate and 30 ml HI (57 wt% in water) were mixed in 100 ml ethanol at 0 °C for 2 h. After reacting the solution of $HC(NH_2)_2I$ was dried with rotary evaporator at 50 °C for 1 h The white crystals were obtained following recrystallization from ethanol and washing with diethyl ether. (b) To obtain CH_3NH_3Br, the mixture solution of 11 ml methylamine (33 wt% in water) and 10 ml HBr (48 wt% in water) were stirred in 100 ml ethanol at 0 °C for 2 h.

(2) Preparation of perovskite absorption solutions. To prepare 1.2 M $HC(NH_2)_2PbI_3$ solution, $HC(NH_2)_2I$ and PbI_2 were dissolved at room temperature in dimethylformamide (DMF) : dimethyl sulfoxide mixed solvent (1 : 0.25 (v/v)). To fabrication of CH_3NH_3Br solution, the sequence of work was the same manner as described above. After preparing of base solution, 0.85 ml of $HC(NH_2)_2PbI_3$ and 0.15 ml of $CH_3NH_3Br_3$ solution were mixed to obtain $(HC(NH_2)_2PbI_3)_{0.85}(CH_3NH_3PbBr_3)_{0.15}$ mixed solution and extra PbI_2 (5 mol% to $HC(NH_2)_2PbI_3$) were added heating at 60 °C for 30 min.

Fabrication of perovskite solar cells. The used photovoltaics devices were fabricated with the following structures, FTO/c-TiO_2/m-TiO_2/perovskite/sprio-OMeTAD/Au. The procedure for cleaning the substrate included sonication and rinsing in distilled water, acetone, and isopropyl alcohol. About 50 nm of compact TiO_2 (c-TiO_2) was deposited by spray pyrolysis with 20 mM titanium diiopropoxide bis(acetylacetonate) solution at 450 °C on FTO substrate. 150 mg ml^{-1} of mesoporous TiO_2 (m-TiO_2, Dysol 30 NR-D) in ethanol was coated at 5000 rpm (acceleration of 2000 rpm s^{-1}) for 10 s and heated 100 °C for 10 min. After process, the substrate was sintered at 500 °C for 30 min. The mixed perovskite solution described above was spin-coated at 2000 rpm (acceleration of 200 rpm s^{-1}) for 10 s followed by 6000 rpm (acceleration of 2000 rpm s^{-1}) for 30 s. During the last 20 s of the second coating steps, the cholorobenzene (CB), which works as anti-solvent, dropped. The perovskite film was heated at 100 °C for 20 min. A solution including 41.6 mg of spiro-OMeTAD, 7.5 μL of 500 mg ml^{-1} lithium bis(trfluoromethylsulphonyl)-imide (Li-TFSI) in acetonitrile (ACN) and 16. 9 μL of 4-*tert*-butylpyridine (*t*BP) in 0.5 ml of CB was dropped and coated on the perovskite layer at 2000 rpm (acceleration of 1200 rpm s^{-1}) for 20 s. 100 nm of Au contacts were formed sequentially by vacuum deposition.

Characterization and stability test of PSCs. The film thickness of AlO_x was measured using a spectroscopic ellipsometer (model: Elli-SE). To confirm the crystallinity of the film, the determined X-ray diffraction (XRD) patterns were measured using XRD-6100 (SHIMADZU, JAPAN) with a Cu Kα radiation source ($\lambda = 0.1541$ nm) at 30 kV and 30 mA. X-ray photoelectron spectroscopy (XPS) was performed using (Thetaprobe XPS, Thermo-Fisher Scientific) with Al Kα source at 15 kV to analyze the chemical bonding and composition of the film. The measured XPS data was calibrated using C 1s peak with 284.6 eV. The contact angle and surface tension values were measured with Phoenix 300 from SEO Co., Ltd., using DI and diiodomethane. The surface energy was determined by the Owen–Wendt equation using two measuring liquids.[63]

$$\gamma_{\mathrm{L}}(1 + \cos\theta) = 2(\gamma_{\mathrm{S}}^{\mathrm{d}}\gamma_{\mathrm{L}}^{\mathrm{d}})^{1/2} + (\gamma_{\mathrm{S}}^{\mathrm{p}}\gamma_{\mathrm{L}}^{\mathrm{p}})^{1/2}, \quad (3)$$

where θ is the measured contact angle of the measuring liquid on the surface, the dispersion and polarity components of water are $\gamma_{\mathrm{L}}^{\mathrm{d}} = 22.85$ dyn cm^{-1} and $\gamma_{\mathrm{L}}^{\mathrm{p}} = 50.3$ dyn cm^{-1}, respectively, and the components of diiodoemethane are $\gamma_{\mathrm{L}}^{\mathrm{d}} = 48.5$ dyn cm^{-1} and $\gamma_{\mathrm{L}}^{\mathrm{p}} = 2.3$ dyn cm^{-1}

To perform TEM, samples mounted on Cu girds were fabricated using a focused ion beam. The prepared sample was measured with JEM-2100F (JEOL Ltd) operating at 200 kV equipped with EDS (TEM 250, Oxford Instruments). The current density–voltage measurements were obtained by the solar cell testing system (LAB 200, McScience, Korea) including simulated solar light (AM 1.5G) with an intensity of 100 mW cm^{-2} using the K3000 model (McScience) and recorder using the ADCMT 6244 source measure unit. After masking with 0.075 cm^2 aperture, the solar cells were measured at a scan rate of 1.2 V s^{-1}. All the results were obtained under ambient conditions. The illumination intensity was calibrated using a standard Si reference

cell (K801S-K067, McScience, Korea). The perovskite solar cell stability test was conducted at 45 °C-65% RH (TH401HA, ETAC, Japan).

Conflicts of interest

There are no conflicts to declare.

Acknowledgements

This research was supported by the Technology Development Program to Solve Climate Changes of the National Research Foundation (NRF) funded by the Ministry of Science and ICT (No. 2017M1A2A2048905), and the New & Renewable Energy of the Korea Institute of Energy Technology Evaluation and Planning (KETEP) grant funded by the Ministry of Trade, Industry and Energy (MOTIE) (No. 20173010012970).

Notes and references

1 J. H. Noh, S. H. Im, J. H. Heo, T. N. Mandal and S. I. Seok, *Nano Lett.*, 2013, **13**, 1764–1769.
2 J. M. Frost, K. T. Butler, F. Brivio, C. H. Hendon, M. Van Schilfgaarde and A. Walsh, *Nano Lett.*, 2014, **14**, 2584–2590.
3 J. Cao, J. Yin, S. Yuan, Y. Zhao, J. Li and N. Zheng, *Nanoscale*, 2015, **7**, 9443–9447.
4 T. Leijtens, G. E. Eperon, N. K. Noel, S. N. Habisreutinger, A. Petrozza and H. J. Snaith, *Adv. Energy Mater.*, 2015, **5**, 1500963.
5 Y. Han, S. Meyer, Y. Dkhissi, K. Weber, J. M. Pringle, U. Bach, L. Spiccia and Y.-B. Cheng, *J. Mater. Chem. A*, 2015, **3**, 8139–8147.
6 H. Kim, K.-G. Lim and T.-W. Lee, *Energy Environ. Sci.*, 2016, **9**, 12–30.
7 X. Dong, X. Fang, M. H. Lv, B. C. Lin, S. Zhang, J. N. Ding and N. Y. Yuan, *J. Mater. Chem. A*, 2015, **3**, 5360–5367.
8 L. Shi, T. L. Young, J. Kim, Y. Sheng, L. Wang, Y. F. Chen, Z. Q. Feng, M. J. Keevers, X. J. Hao, P. J. Verlinden, M. A. Green and A. W. Y. Ho-Baillie, *ACS Appl. Mater. Interfaces*, 2017, **9**, 25073–25081.
9 S. N. Habisreutinger, T. Leijtens, G. E. Eperon, S. D. Stranks, R. J. Nicholas and H. J. Snaith, *Nano Lett.*, 2014, **14**, 5561–5568.
10 A. Y. Mei, X. Li, L. F. Liu, Z. L. Ku, T. F. Liu, Y. G. Rong, M. Xu, M. Hu, J. Z. Chen, Y. Yang, M. Gratzel and H. W. Han, *Science*, 2014, **345**, 295–298.
11 I. Hwang, I. Jeong, J. Lee, M. J. Ko and K. Yong, *ACS Appl. Mater. Interfaces*, 2015, **7**, 17330–17336.
12 H. C. Weerasinghe, Y. Dkhissi, A. D. Scully, R. A. Caruso and Y.-B. Cheng, *Nano Energy*, 2015, **18**, 118–125.
13 Q. Dong, F. Liu, M. K. Wong, H. W. Tam, A. B. Djurišić, A. Ng, C. Surya, W. K. Chan and A. M. C. Ng, *ChemSusChem*, 2016, **9**, 2597–2603.
14 F. Matteocci, L. Cinà, E. Lamanna, S. Cacovich, G. Divitini, P. A. Midgley, C. Ducati and A. Di Carlo, *Nano Energy*, 2016, **30**, 162–172.
15 L. Wang, C. Ruan, M. Li, J. Zou, H. Tao, J. Peng and M. Xu, *J. Mater. Chem. C*, 2017, **5**, 4017–4024.
16 T. Nam, Y. J. Park, H. Lee, I.-K. Oh, J.-H. Ahn, S. M. Cho, H. Kim and H.-B.-R. Lee, *Carbon*, 2017, **116**, 553–561.
17 E. Y. Choi, J. Kim, S. Lim, E. Han, A. W. Ho-Baillie and N. Park, *Sol. Energy Mater. Sol. Cells*, 2018, **188**, 37–45.
18 M.-H. Park, J.-Y. Kim, T.-H. Han, T.-S. Kim, H. Kim and T.-W. Lee, *Adv. Mater.*, 2015, **27**, 4308–4314.
19 H.-K. Seo, M.-H. Park, Y.-H. Kim, S.-J. Kwon, S.-H. Jeong and T.-W. Lee, *ACS Appl. Mater. Interfaces*, 2016, **8**, 14725–14731.
20 Z. Liu, B. Sun, T. Shi, Z. Tang and G. Liao, *J. Mater. Chem. A*, 2016, **4**, 10700–10709.
21 X. Ling, C. Ser Choong, C. S. Premachandran, D. Pinjala and M. K. Iyer, *7th Electronic Packaging Technology Conference (EPTC)*, 2005, vol. 1, p. 5.
22 M. C. Bélanger and Y. Marois, *J. Biomed. Mater. Res.*, 2001, **58**, 467–477.
23 S. H. Jeong, S. Zhang, K. Hjort, J. Hilborn and Z. Wu, *Adv. Mater.*, 2016, **28**, 5830–5836.
24 X. Liu, Y. Xu, K. Ben, Z. Chen, Y. Wang and Z. Guan, *Appl. Surf. Sci.*, 2015, **339**, 94–101.
25 M. Tovar, T. Weber, S. Hengoju, A. Lovera, A.-S. Munser, O. Shvydkiv and M. Roth, *Biomicrofluidics*, 2018, **12**, 024115.
26 J. Wang, S. Wang, P. Zhang and Y. Li, *18th International Conference on Electronic Packaging Technology (ICEPT)*, 2017, vol. 1, pp. 1051–1055.
27 C. Wu, T. G. Lin, Z. Zhan, Y. Li, S. C. H. Tung, W. C. Tang and W. J. Li, *Microsyst. Nanoeng.*, 2017, **3**, 16084.
28 S. H. Kim, J.-H. Moon, J. H. Kim, S. M. Jeong and S.-H. Lee, *Biomed. Eng. Lett.*, 2011, **1**, 199.
29 S. Sonney, N. Shek and J. M. Moran-Mirabal, *Biomicrofluidics*, 2015, **9**, 026501.
30 S. Martin and B. Bhushan, *J. Colloid Interface Sci.*, 2017, **488**, 118–126.
31 J. Niinistö, Atomic Layer Deposition of High-k Dielectrics from Novel Cyclopentadienyl-Type Precursors, Doctor's dissertation, Helsinki University of Technology, Otaniemi, Helsinki, 2006.
32 W. Lu, Y. Iwasa, Y. Ou, D. Jinno, S. Kamiyama, P. M. Petersen and H. Ou, *RSC Adv.*, 2017, **7**, 8090–8097.
33 J. Haeberle, K. Henkel, H. Gargouri, F. Naumann, B. Gruska, M. Arens, M. Tallarida and D. Schmeißer, *Beilstein J. Nanotechnol.*, 2013, **4**, 732–742.
34 T. Van Khai, H. G. Na, D. S. Kwak, Y. J. Kwon, H. Ham, K. B. Shim and H. W. Kim, *J. Mater. Chem.*, 2012, **22**, 17992–18003.
35 J. G. Lee, H. G. Kim and S. S. Kim, *Thin Solid Films*, 2015, **577**, 143–148.
36 A. Bulusu, A. Singh, C. Y. Wang, A. Dindar, C. Fuentes-Hernandez, H. Kim, D. Cullen, B. Kippelen and S. Graham, *J. Appl. Phys.*, 2015, **118**, 085501.
37 K. H. Yoon, H. S. Kim, K. S. Han, S. H. Kim, Y.-E. K. Lee, N. K. Shrestha, S. Y. Song and M. M. Sung, *ACS Appl. Mater. Interfaces*, 2017, **9**, 5399–5408.
38 T. Bülow, H. Gargouri, M. Siebert, R. Rudolph, H.-H. Johannes and W. Kowalsky, *Nanoscale Res. Lett.*, 2014, **9**, 223.

39 L. Lee, K. H. Yoon, J. W. Jung, H. R. Yoon, H. Kim, S. H. Kim, S. Y. Song, K. S. Park and M. M. Sung, *Nano Lett.*, 2018, **18**, 5461–5466.
40 J. C. Spagnola, B. Gong, S. A. Arvidson, J. S. Jur, S. A. Khan and G. N. Parsons, *J. Mater. Chem.*, 2010, **20**, 4213–4222.
41 J. M. Mohr and D. R. Paul, *J. Appl. Polym. Sci.*, 1991, **42**, 1711–1720.
42 V. Compañ, A. Andrio, M. L. López, C. Alvarez and E. Riande, *Macromolecules*, 1997, **30**, 3317–3322.
43 N. Bosq, N. Guigo, J. Persello and N. Sbirrazzuoli, *Phys. Chem. Chem. Phys.*, 2014, **16**, 7830–7840.
44 A. Bulusu, S. Graham, H. Bahre, H. Behm, M. Böke, R. Dahlmann, C. Hopmann and J. Winter, *Adv. Eng. Mater.*, 2015, **17**, 1057–1067.
45 M. A. Mendez and V. A. Szalai, *Nanoscale Res. Lett.*, 2013, **8**, 210.
46 D. N. Goldstein, J. A. McCormick and S. M. George, *J. Phys. Chem. C*, 2008, **112**, 19530–19539.
47 S. Armyanov, N. E. Stankova, P. A. Atanasov, E. Valova, K. Kolev, J. Georgieva, O. Steenhaut, K. Baert and A. Hubin, *Nucl. Instrum. Methods Phys. Res., Sect. B*, 2015, **360**, 30–35.
48 S. R. Saptarshi, A. Duschl and A. L. Lopata, *J. Nanobiotechnol.*, 2013, **11**, 26.
49 G. N. Parsons, S. E. Atanasov, E. C. Dandley, C. K. Devine, B. Gong, J. S. Jur, K. Lee, C. J. Oldham, Q. Peng, J. C. Spagnola and P. S. Williams, *Coord. Chem. Rev.*, 2013, **257**, 3323–3331.
50 C. A. Wilson, R. K. Grubbs and S. M. George, *Chem. Mater.*, 2005, **17**, 5625–5634.
51 J. Wang, T. Pan, J. Zhang, X. Xu, Q. Yin, J. Han and M. Wei, *RSC Adv.*, 2018, **8**, 21651–21657.
52 Z. Huang, F. Wang and J. Li, *11th International Conference on the Properties and Applications of Dielectric Materials (ICPADM)*, 2015, vol. 1, pp. 293–296.
53 H.-Y. Li, Y.-F. Liu, Y. Duan, Y.-Q. Yang and Y.-N. Lu, *Materials*, 2015, **8**, 600.
54 T. Ohishi, Y. Yamazaki and T. Nabatame, *Frontiers in Nanoscience and Nanotechnology*, 2016, **2**(4), 149–154.
55 S. Park, L. H. Kim, Y. J. Jeong, K. Kim, M. Park, Y. Baek, T. K. An, S. Nam, J. Jang and C. E. Park, *Org. Electron.*, 2016, **36**, 133–139.
56 W. M. Yun, J. Jang, S. Nam, Y. J. Jeong, L. H. Kim, S. Park, S. J. Seo and C. E. Park, *J. Mater. Chem.*, 2012, **22**, 25395–25401.
57 B. M. Henry, A. G. Erlat, A. McGuigan, C. R. M. Grovenor, G. A. D. Briggs, Y. Tsukahara, T. Miyamoto, N. Noguchi and T. Niijima, *Thin Solid Films*, 2001, **382**, 194–201.
58 Y. Y. Tomoji Ohishi, *Mater. Sci. Appl.*, 2017, 1–14.
59 T. Ohishi and K. Yanagida, *Frontiers in Nanoscience and Nanotechnology*, 2016, **2**(5), 173–178.
60 S.-H. Schulze, C. Ehrich, R. Meitzner and M. Pander, *Prog. Photovoltaics*, 2017, **25**, 1051–1058.
61 J. Kim, N. Park, J. S. Yun, S. Huang, M. A. Green and A. W. Y. Ho-Baillie, *Sol. Energy Mater. Sol. Cells*, 2017, **162**, 41–46.
62 R. Paetzold, A. Winnacker, D. Henseler, V. Cesari and K. Heuser, *Rev. Sci. Instrum.*, 2003, **74**, 5147–5150.
63 D. Hong, K. Bae, S.-P. Hong, J. H. Park, I. S. Choi and W. K. Cho, *Chem. Commun.*, 2014, **50**, 11649–11652.